Operando spectroscopic studies of alcohol to hydrocarbon process over HSSZ-13 with the aid of MCR-ALS analysis for active species identification

Anna Walczyk, Karolina A. Tarach*, Agata Kordek, Agata Olszewska, Oliwia Rogala, Kinga Góra-Marek

Faculty of Chemistry, Jagiellonian University in Kraków, Gronostajowa 2, 30-387 Kraków, Poland

corresponding author: Karolina A. Tarach; karolina.tarach@uj.edu.pl

Abstract

This research examines the conversion of C_1 and C_2 alcohols to higher olefins utilizing protonic chabazite (HSSZ-13, Si/Al = 11) zeolite. The study employs advanced *operando* spectroscopy techniques, including FT-IR and UV-vis, while simultaneously using mass spectrometry and gas chromatography to analyze the products. By applying identical amounts of C_1 and C_2 alcohols, the research can effectively examine the intermediates formed and coke production. Further, the same zeolite structure aids a more comprehensive understanding of reaction pathways. The *operando* FT-IR and UV-vis studies supplemented by mass spectrometry and gas chromatography results for products released from the catalyst surface provide significant information on the key intermediates involved. The similarities and discrepancies between the transformation of ethanol and methanol into olefins, according to the established hydrocarbon pool process, are noted. MCR-ALS analysis is employed for the *operando* FT-IR and UV-vis the results, providing significant insights into the findings. Additionally, the research is supported by chromatographic examinations of the coke species obtained from spent catalysts.

Keywords: hydrocarbon pool, zeolite, alcohol conversion, operando, MCR-ALS

1. Introduction

Production of a wide range of valuable chemicals with diverse applications frequently begins with ethylene and propylene as key substrates in various petrochemical processes. As a result, these two olefins are among the most essential raw materials in the chemical industry, with their demand increasing each year [1 and references therein]. Consequently, there is a growing need to develop new, more sustainable methods for their production. Currently, they are mainly obtained through steam cracking of naphtha or fluid catalytic cracking of crude oil processes, which operate under harsh conditions and rely on non-renewable resources [1], which results in significant energy consumption and comparatively low yields of desired products. In order to lessen the environmental impact of industrial processes, worldwide search for more sustainable, i.e., environmentally friendly and benign ways of olefin production are sought.

Hence, alcohols, such as ethanol or methanol, were successfully applied for olefin production, with methanol-to-hydrocarbon transformations over ZSM-5 catalysts already being commercialized [2]. It is well established that alcohols can be produced from bio-resources, mainly through biomass valorization [3, 4]. Despite being extensively investigated and industrially applied, alcohol transformation mechanisms remain unclear. It is generally agreed upon that the conversion of alcohols on zeolites occurs via the "hydrocarbon pool" (HPC) mechanism [5-8], postulated by Dahl and Kolboe over 30 years ago [9]. However, its course is not precisely established; hence, it remains a matter of scientific debate. Ethanol transformation on zeolites is widely recognized to yield HP alongside a concurrent dehydration reaction, which remains a substantial component of the process. In both methanol-to-hydrocarbons (MTH) and ethanol-to-hydrocarbons (ETH) reactions, polymethylated cyclopentenyl and benzenium cations have been identified to be among crucial intermediates in HP that give rise to light olefins and coke precursors [10-13].

Catalysts that can convert low alcohols while achieving high yields under mild reaction conditions are in demand globally. Most solid acid catalysts examined for the MTH process focus on the commercially available SAPO-34 zeotype material [14-16]. However, ZSM-5 has attracted more significant interest in studies of ethanol transformations, particularly regarding dehydration. Compared with the MTH outcome, chabazite-type catalysts have also been investigated for ETH [17], [18-24]. The chabazite framework facilitates the selective diffusion of generated light olefins via its narrow channels; nevertheless, the presence of expansive chabazite cages permits the formation of larger molecules, such as alkylated polyaromatic or polycyclic species, which are unable to leave. These deposits, primarily composed of coke, are mainly accountable for the deactivation of the catalyst [25-29].

Various approaches were employed to monitor the alcohol's reaction pathway, with *operando* mode spectroscopies such as IR and/or UV-Vis proving the most informative [11, 30-35]. The *operando* approach provides a more comprehensive understanding of the reaction mechanism through frequent data collection, enabling the observation of sequential changes that intermediate species experience during the process. Additionally, applying the multivariate curve resolution–alternating least squares (MCR–ALS) spectral data analysis method provides a deeper insight into the reaction path.

While many studies focused on the ethanol-to-hydrocarbons (ETH) process, the complete conversion process of ethanol has rarely been examined using the *operando* approach. Additionally, the specific active intermediates and the detailed production pathways for light olefins, particularly propylene, are not yet fully understood.

2. Experimental

2.1. Materials

The experiment employed commercially available zeolite SSZ-13 (ACS Material LLC, Pasadena, CA, USA) with a CHA topology. The samples used in the experiments were calcined beforehand at 550 °C for 3 hours.

2.2. Chemical composition, structural and textural parameters of the studied sample

The chemical composition of the catalyst was determined via inductively coupled plasma optical emission spectrometry (ICP-OES, Optima 2100DV, PerkinElmer, Waltham, MA, USA). Powder X-ray diffraction pattern was recorded with Rigaku Multiflex diffractometer using Cu Kα radiation (40 kV, 40 mA). Nitrogen adsorption/desorption experiments were conducted using a Quantachrome Autosorb 1-MP gas sorption analyzer for porosity characterization. The sample was degassed at 10^{-5} bar at 350 °C for 24 h before measurement. The specific surface area, S_{BET}, was calculated using the Brunauer–Emmett–Teller formalism. The micropore volume (V_{micro}) was calculated using the t-plot method.

2.3. Acidic sites characterization with FT-IR *in situ* spectroscopic studies

The acidic properties of the protonic sample were investigated in quantitative FT-IR ammonia (NH_3) sorption experiments to probe the Brønsted and Lewis acid sites. The samples of pure zeolites were pressed into self-supported discs without adding any other compounds and then placed in a custom-made thermoregulated quartz infrared cell. In situ evacuation at 550 °C under a high vacuum (10^{-5} mbar) for 1 h was performed to remove any adsorbed species. The probe molecules were introduced after cooling to 200 °C for NH_3 sorption experiments. To probe all acid sites, the sorption of NH_3 excess was conducted at 200 °C under static conditions. Next, the gaseous and physisorbed molecules were removed by desorption at 200 °C. These spectra were used to quantitatively assess Brønsted and Lewis acid site concentrations employing respective absorption coefficients [36]. All spectra presented in this work were recorded by gathering 100 scans with a spectral resolution of 2 cm^{-1} on a Vertex 70 spectrometer (Bruker) equipped with an MCT detector.

2.4. UV-Vis and FT-IR *operando* spectroscopic studies coupled with Gas Chromatography and Mass spectrometry measurements during alcohol conversion over chabazite zeolite

Before the operando spectroscopic experiments, a catalyst self-supported disc (~25 mg) was placed in a 2 cm^3 volume quartz IR cell (Polish Patent Pat.232633, Cracow, Poland), where it was pre-treated under continuous helium flow for 60 min at 550 °C. The setup was then cooled to a reaction temperature of 325 °C. Then, helium carrier gas was passed over liquid methanol or ethanol (analytical grade, 99% purity), contained in a vessel placed in a heating circulation bath (Huber, Germany) set at −0.7 °C for methanol which gave WHSV = 5 h^{-1} or 14 °C for ethanol, which gave WHSV = 7 h^{-1}. The total flow rate of the feed stream was kept at 40 $mL \cdot min^{-1}$. The reaction run was investigated with an operando system connected to a flow setup. IR spectra were collected with an Invenio X Bruker spectrometer equipped with an MCT detector. The spectral resolution was 2 cm^{-1}. Analogously, for UV–Vis (Shimadzu UV-2600, Shimadzu Corporation, Kyoto, Japan) experiments, the catalysts were prepared in a self-supported pellet form (~25 mg) and placed in a Praying Mantis® cell. They were then pre-treated at 500 °C for 60 min. UV-Vis spectra were recorded in operando mode at the reaction temperature of 325 °C. Products were simultaneously analyzed via mass spectrometry (MeasLine, www.measline.com, RGA200, Cracow, Poland) and gas chromatography (Agilent Technologies 7890B, Agilent Technologies, Santa Clara, CA, USA).

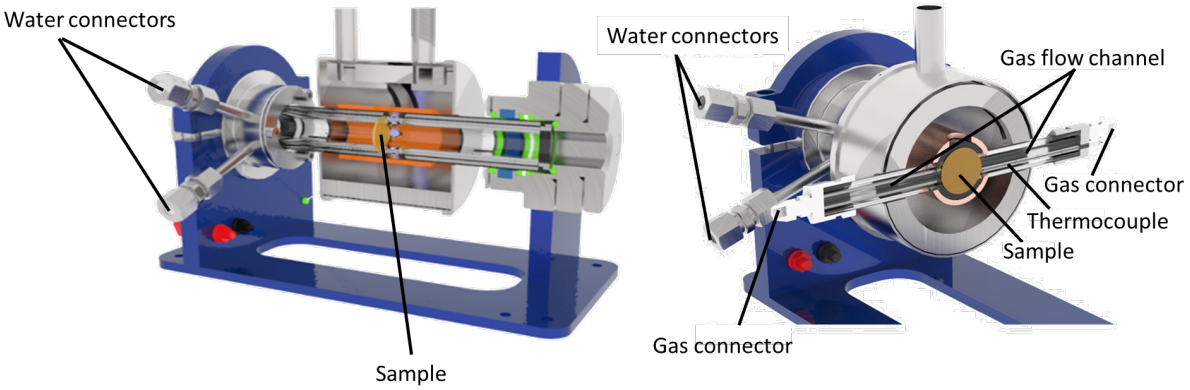

Scheme 1. Cross-section view of the FT-IR spectroscopic cell used in *operando* study.

2.5. MCR-ALS analysis of spectroscopic data

The multivariate curve resolution-alternating least-squares (MCR-ALS) algorithm analysis was applied to distinguish the concentration profiles and pure spectra for spectroscopically active components during methanol and ethanol transformation over the catalysts studied. MCR-ALS analysis was applied for the UV-Vis spectra, and the IR spectral region was analyzed in the area of C-C and C-H deformation modes (1700 – 1300 cm^{-1}). The analysis was performed using the toolbox provided in the MATLAB graphical user interface [37-39]. The singular value decomposition (SVD) algorithm was used to estimate the appropriate number of components describing the ethanol catalytic transformations. Non-negativity, unimodality, and equality constraints were also applied during the analysis. The MCR-ALS algorithm iteratively optimized initial estimates for each spectrum and coverage until the convergence criterion 10^{-6} was achieved.

2.6. Coke analysis with GC-MS and TG analysis of extracted species from spent catalyst

For GC-MS analysis, the spent zeolite (around 16 mg) was put in a Teflon container and mixed with hydrofluoric acid (HF, 40%, Honeywell Fluka, 1 mL), and then the mixture was left for 1 hour. Following the zeolite dissolution, the solution of boric acid (H_3BO_3, 20%, Honeywell Fluka, 6 mL) was added, and after another hour, the coke extraction was conducted using 1 g of dichloromethane (CH_2Cl_2, Sigma-Aldrich). The GC–MS analysis was performed using an 8890B gas chromatograph with a 7693 autosampler and a 5977B mass-selective detector (Agilent Technologies). The conditions of the analysis of the coke contents are outlined in Table S2. The chromatograms with mass spectroscopy results were analyzed using the MassHunter Qualitative Analysis 10.0 software, and for the extracted species identification, NIST 20 Mass Spectral Library was used.

Spent catalysts were grounded in an agate mortar and subjected to coke analysis. The total amount of coke was evaluated using TG analysis with synthetic air flow. For this purpose, a portion of ~5 mg of the catalyst in powder form was loaded into an 85 µL α-Al_2O_3 crucible and weighted with a NETZSCH STA 449 F5 Jupiter thermobalance (Netzsch-Gerätebau GmbH, Selb, Germany) before the analysis. The coke content of the spent catalysts was measured in TG experiments where the temperature was raised to 800 °C with a rate of 10 °C·min^{-1}, and synthetic air flow was set at 100 mL·min^{-1}.

3. Results and discussion

3.1. Chemical, structural, and textural characterization of studied chabazite zeolite

Figure 1 presents the isotherm and XRD diffractogram for the studied SSZ-13. Table 1 gathers the data obtained during chemical analysis, the nitrogen sorption/desorption results, and the acidity characterization of the studied catalyst.

The SSZ-13 material was characterized by a large BET surface area of 812 $m^2 \cdot g^{-1}$ and a micropore volume of 0.31 $cm^3 \cdot g^{-1}$. The shape of the isotherm pointed to the well-developed microporosity of the material. The X-ray diffraction analysis result demonstrated a characteristic pattern of the well-crystalline chabazite framework structure. Ammonia sorption experiments revealed a moderate Brønsted acidity of the catalyst.

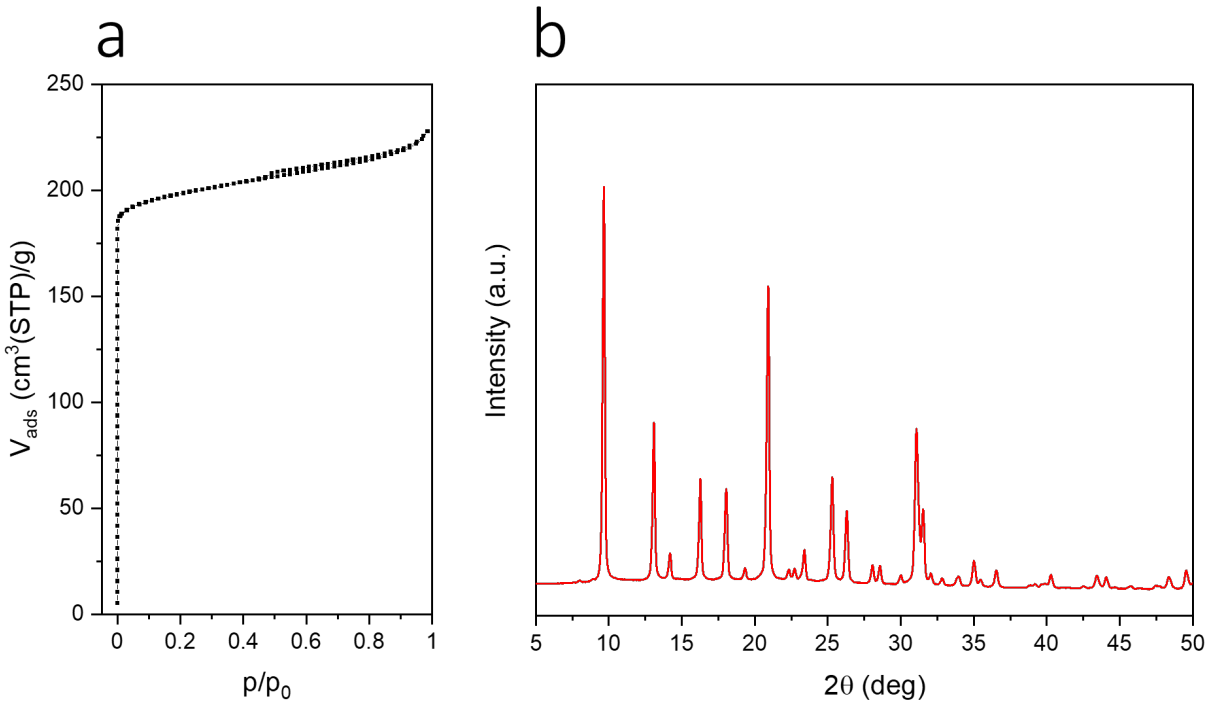

Figure 1 Left: Isotherm of low-temperature nitrogen sorption/desorption experiment. Right: X-ray diffraction pattern of studied zeolite.

Table 1 Chemical, textural, and acidic characteristics of the studied catalyst.

Sample	Si/Al	S_{BET} ($m^2 \cdot g^{-1}$)	V_{micro} ($cm^3 \cdot g^{-1}$)	Acid sites concentration (µmol·g^{-1})	
				BAS (NH_4^+)	LAS (NH_3L)
SSZ-13	11	812	0.31	760	10

3.2. UV-Vis and FT-IR *operando* spectroscopic studies coupled with GC-MS analysis during the transformation of alcohols

UV-Vis spectroscopy allowed for differentiation between ionic and neutral species adsorbed on the catalyst's surface and for tracking changes these species underwent during two hours of the reaction. Spectra collected for methanol or ethanol transformations conducted at 325 °C are presented in Figures 2a and 2b.

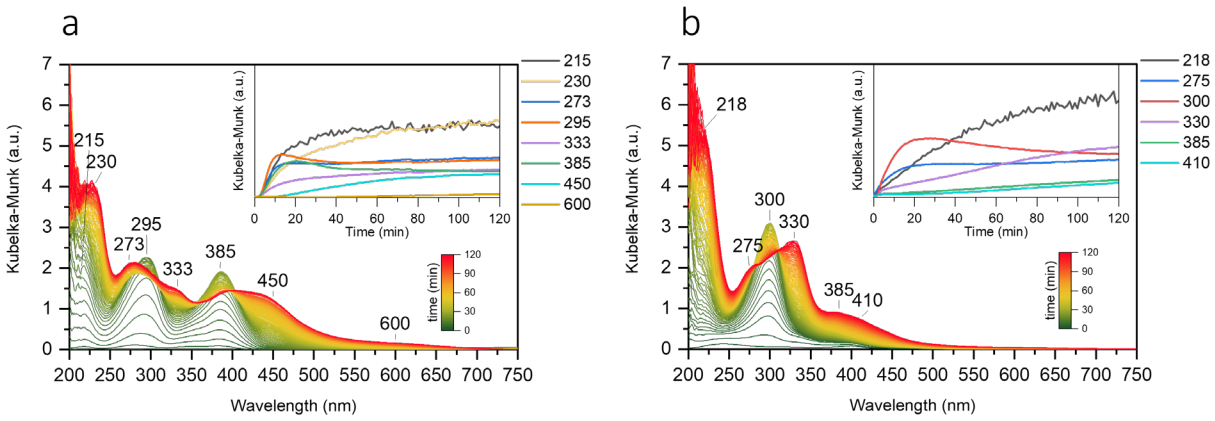

Figure 2 UV-Vis spectra registered during a) methanol and b) ethanol transformation reactions. Insets: time traces of specific bands.

The initial stage in the MTH and MTO processes is characterized by an induction period with a low methanol conversion rate. Several factors are suggested to influence the induction period, such as the presence of steam and a high reactant contact time. Water competes with methanol and dimethyl ether for adsorption on zeolite active sites, influencing the reverse reaction from methoxy species to methanol, thus limiting reaction progress. However, water can also stabilize specific carbocationic intermediates essential to the MTH process [40, 41]. With respect to its pore architecture, the H-SAPO-34 zeotype of the CHA framework can limit the diffusion of hydrocarbons because of its small pores and accelerate the formation of the "hydrocarbon pool". The induction period reduces with increased temperature and pressure [42]. Consequently, the experiments performed at low temperatures and low pressure elucidate the fundamental steps of the induction period in MTO, MTH, and ETH conversion.

For the SSZ-13 catalyst, the first 20 minutes of the MTH reaction (Figure 2a) constituted its induction period and most active part, as the intense rising of 215 nm, 295 nm, and 385 nm bands could be observed, pointing to the formation of a variety of products, among which intermediate species were distinguished. The former band continued to grow steadily throughout the process, although at a decreasing rate than initially. Development of the 295 nm band stopped at ca. 15 minutes of the experiment and started to decline mildly. Similar behavior was observed for the 385 nm signal, the growth of which was suppressed slightly later, at ca. 20 minutes. Then, at the expense of the 295 and 385 nm bands, the 333 and 450 nm bands of aromatic-derived species emerged and persisted in their modest growth. The behavior observed for 295 and 385 nm bands allowed us to assign them to intermediate species. Rapid initialization of the hydrocarbon pool when methanol was the substrate was manifested by the higher abundance of intermediate polyalkylated cyclopentenyl cations (273 nm), which were produced when the olefin (propylene) molecule was released [10]. As the band at 273 nm was formed at the expense of 295 and 385 nm bands, it should also indicate the involvement of the polyalkylated cyclopentenyl cations in the deactivation process. At the final stage (Figure 2a, inset), the 600 nm band originating from pyrenic or graphitic species was formed.

For the ETH reaction at SSZ-13 (Figure 2b), the picture of the UV-Vis bands development differed in some aspects from the MTH process. Consequently, bands of short olefinic species (218 nm) and polyalkylated cyclopentenyl cations (300 nm) intensified significantly within the initial 20 minutes of the reaction. After this time, the 300 nm band started to decrease slowly, followed by the appearance of the bands at 275, 330, 385, and 410 nm. During the ETH process, the 275 nm signal appeared later than

the analogous 273 nm signal in the MTH reaction, where it could be noticed yet after ca. 20 minutes, disguised under a broadened 295 nm signal. In the later stages, in contrast to the MTH reaction, the signal 385 nm grew steadily throughout the experiment. In the ETH case, the 385 nm band could not be ascribed to intermediate species, as in MTH. Also, the 600 nm band could not be clearly detected.

Table 2 presents the assignment of the bands to specific hydrocarbon compounds based on experimental data with the aid of the literature reports.

Table 2 Assignment of signals observed during UV-Vis *operando* experiments to specific compounds.

Wavelength (nm)	Assignment	Ref.
215 218	light olefins	[11]
230	neutral aromatic species	[43]
273 275	polyalkylated cyclopentenyl cations (intermediate species) with lower amounts/shorter substituting groups	[11],[10]
295 300	polyalkylated cyclopentenyl cations (intermediate species) with higher amounts/longer/branched substituting groups	[11],[10]
333 330	tri(m)ethyl benzenes	This work
385	polyalkylated (hexamethylated) benzenium cations	[11]
410	naphthalene	[43]
450	(alkylated) naphthalene ions	This work
600	(alkylated) polyarene ions	[2, 30]

For both ethanol and methanol conversion experiments, alkylated cyclopentenyl cations (295 and 300 nm) could be distinguished as one of the key intermediates [44], produced extensively in the first phases of the reaction. Later, at their expense, other hydrocarbon species were created. Importantly, as the 295 nm band reached its maximum, development of the 385 nm signal started, suggesting the relation between these two bands, as was pointed out by Zhang et al. [45]. Both methylated cyclopentenyl cations (295 nm) and polymethylated benzenium cations (385 nm) constitute essential transitional MTH reaction products, transformations of which yield olefins and higher aromatic species that serve as coke precursors, identified by the 450 and 600 nm bands. A similar route occurred for the ETH, with different substituting groups attached to the five- or six-atomic ring cations. This was evidenced by the intense increase of the 300 nm band at the initial reaction stage. From its shape and sharper intensity than the analogous 295 nm MTH band, it can be concluded that cyclopentenyl cations formed in ETH were more homogeneous. Additionally, the cyclopentenyl cations band position shifted to a higher wavelength due to the longer alkyl substituents; most probably, ethyl substituents were prevalent.

In general, operando UV-Vis results illustrated a more efficient activation of the HCP mechanism when methanol was the substrate. Higher efficiency of forming the intermediate species resulted in a broad distribution of the products and elevated coking (bands at 410, 450 nm, and 600 nm). In the ETH reaction, parallel to HCP, a more direct route for producing ethylene, i.e., alcohol dehydration, could be anticipated [8, 46], as the 218 nm band grew extensively for two hours of the experiment.

FT-IR spectra obtained during the transformation of methanol and ethanol under identical conditions as those employed in the operando UV-Vis study are illustrated as top-down projections supported by

the time evolution of the specific bands in Figure 3a-d. Assignment of the bands, based on obtained data and the literature reports [47-52], is presented in Table 3. The main focus was on the 1700-1300 cm^{-1} region, where bands stemming from vibrations of C=C and C-H of hydrocarbonaceous species are present.

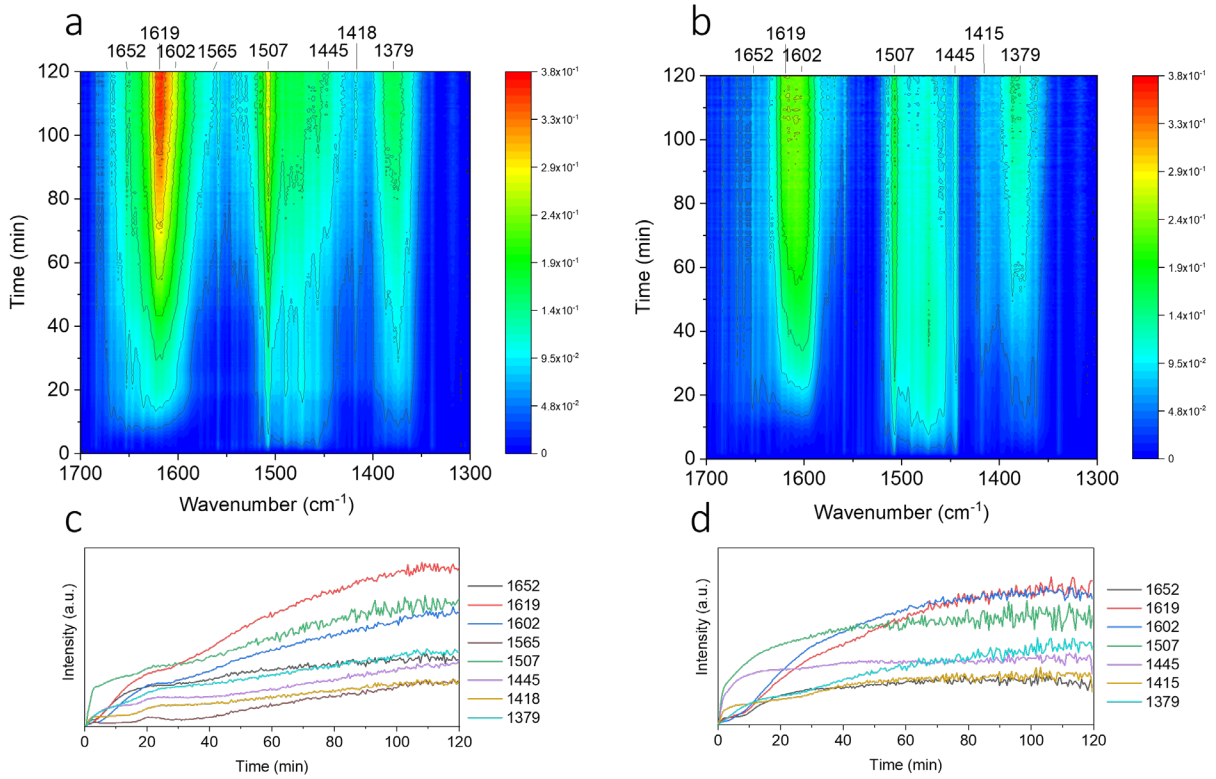

Figure 3 Top-down projections of FT-IR spectra registered during a) methanol and b) ethanol conversion. Time traces of the selected FT-IR bands from c) MTH and d) ETH experiments.

Table 3 Assignment of signals registered during FT-IR *operando* experiments to specific compounds.

Wavenumber (cm^{-1})	Assignment	Ref.
1652	dienes	[10]
1619 / 1620	polyalkylated benzenium cations	[10], [53]
1602	alkylated benzenium cations	[47]
1565	naphthalene	This work
1507	alkylated cyclopentenyl cation	[10]
1445	ethylene	[54]
1418	dimethyl ether	This work
1415	diethyl ether	This work
1379	non-aromatic species; olefins; iso-compounds	[55]

At the early stages of the MTH reaction (Figure 3a), as the first products, polymethylated cyclopentenyl species identified by the 1507 cm^{-1} band were formed. Next, unsaturated hydrocarbons were produced, indicated by the appearance of the vibrations of $–CH_2$ from olefinic and/or aromatic species (1500-1425 cm^{-1}). This effect was followed by developing a complex band located at 1619 cm^{-1}, signifying the presence of either tetramethylbenzenium ions or higher olefins with conjugated double bonds. Further, the rising of the 1379 cm^{-1} band from symmetric in-phase CH_3 deformations pointed to moderate

production of iso-compounds and/or polyalkyl-substituted aromatics. Also, in the latter stages of the process, growth of the 1418 cm^{-1} signal could be observed. All signals mentioned above persisted in their growth.

The 1418 cm^{-1} band may stem from dimethyl ether methoxy group vibrations since the GC measurements confirmed its presence from the beginning of the reaction. Analysis of the spectra recorded during the first 10 minutes of the methanol conversion, in the range 3100-2700 cm^{-1} (Figure S1), allowed for observation of bands characteristic of dimethyl ether compound, namely 2818 and 3010 cm^{-1}, that grew for the first few minutes and later decreased. The mass spectrometry (Figure 4e) results provided similar conclusions: the DME (m/z = 45) was produced in high amounts during the initial reaction period. Thus, the DME, in addition to methanol, served as the leading methylating agent on the catalyst's surface. It was seen as a decrease in IR band intensity after reaching a maximum of 1.5 minutes. However, DME was also an indicator of catalyst deactivation, as its production increased with the coke precursors' poisoning of highly acidic centers. Simultaneously, the production of olefinic species decreased in favor of DME, whose production requires sites of lower strength. Increased coking led to a significant acidity reduction, diminishing the catalyst's activity. However, as pointed out by Liang et al. in the case of MTH reaction [56], methylated naphthalene constitutes an important hydrocarbon pool intermediate that improves the formation of methylated benzenium species. Also, Arivazhagan et al. [51] observed a 1418 cm^{-1} band when studying spectral features of 1,5-dimethyl naphthalene. Hence, naphthalenic compounds could also participate in the 1418 cm^{-1} band. Indeed, as the development of 1418 and 1507 cm^{-1} bands slowed down, the 1619 cm^{-1} band started to increase at a greater rate, indicating persistent, parallel transformations of naphthalene intermediates as well as expansion of the five-atoms cyclopentenyl species into six-atoms benzenium ions. It cannot be excluded that in the latter phases, with progressive coke formation, the 1619 cm^{-1} band growth stemmed mainly from coke species.

For ethanol conversion, the first few minutes of the reaction could also be identified as an induction period, where the significant formation of intermediate polymethylated cyclopentenyl species (1507 cm^{-1}) was observed. This effect was accompanied by a less extensive rising of a 1415 cm^{-1} signal, ascribed analogously to diethyl ether as in the MTH case. The ETH time profiles (Figure 3b and 3d) appeared to exhibit similarities in product signals, with the main difference being the bands' intensities, pointing to a lower excess of coking of the catalyst compared to the MTH reaction. Notably, polymethylated benzenium cations were not detected immediately during the ETH reaction, as these species were generated in smaller quantities than the MTH experiment. Also, earlier rising of the bands near 1445 cm^{-1} and their higher intensity evidenced more extensive olefins production in ETH reaction. In later stages of the reaction, a dependence between the bands at 1415, 1507, and 1619 cm^{-1} was observed, indicating that, although dehydration was critical in the ETH mechanism, pathways analogous to those as in the MTH process contributed to the production of light olefins. It should be noted, though, that the expansion of the cyclopentenyl cation ring to form benzenium cation had a lesser impact on the ETH process, as indicated by UV-Vis results.

The results of the GC-MS analyses provided information on the reaction products desorbed from the catalyst surface. Product selectivities, together with MS results, are presented in Figure 4.

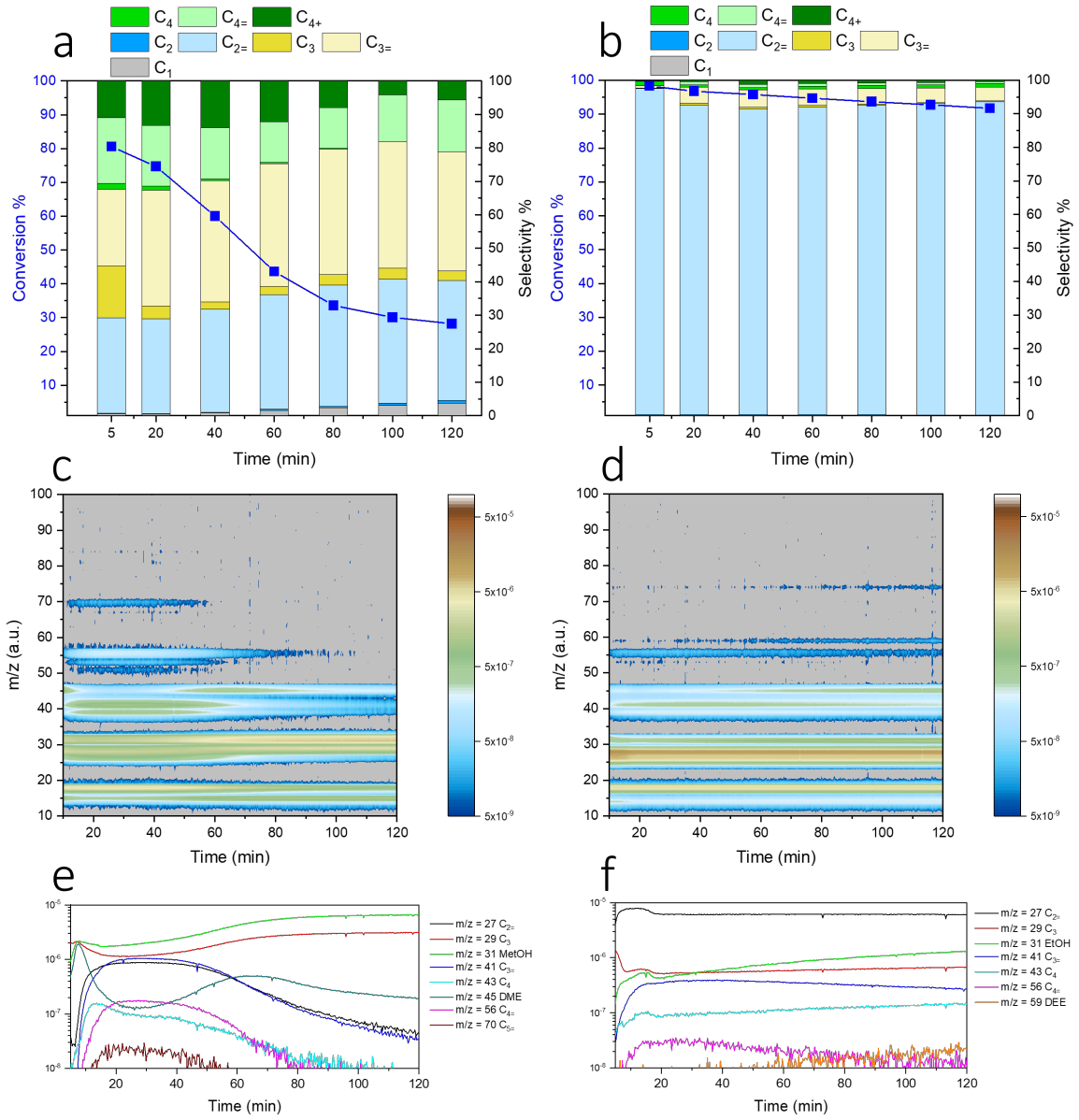

Figure 4 GC-MS results collected during operando UV-Vis experiments: (a, b) conversion and selectivities obtained during methanol and ethanol conversion experiments, respectively; (c, d) mass spectra with selected mass traces (e, f) obtained during methanol and ethanol conversion experiments, respectively; DME – dimethyl ether; DEE – diethyl ether.

Thus, during the MTH process (Figure 4a), substrate conversion slowly declined in the first phase, from 80% to 75%, to a later drop, especially between 20 and 80 minutes, and reached 28% at the end of the experiment. The product distribution was diversified with favorable C_2, C_3, and C_4 olefins production. In the initial reaction stage, propane, C_{4+} products, and a small amount of methane could be detected. With the progress of the experiment, the reaction was suppressed. Also, C_4 olefin amounts started to decrease, resulting in ethylene and propylene predominating in the product mixture during the latter half of the process. However, due to the conversion drop caused by the catalyst deactivation, light olefin yields (Figure S3) did not exceed 25% at any reaction stage. In the ETH reaction (Figure 4b), conversion slightly decreased while remaining consistently above 90%. The distribution of products was limited, with ethylene as the primary product exhibiting over 90% selectivity. The selectivity to other olefins was a maximum of 5.1%, with propylene as the main product.

In general, wider product distribution could be seen for the MTH process, stemming from the smaller building block of the C_1 molecule, which apparently activated the HCP mechanism very efficiently. This allowed for diversified production of olefins, a small amount of paraffin, and C_{4+} species. However, it also caused fast deactivation of the catalyst. According to expectations, ethylene production was favorable when ethanol was the starting reagent, as dehydration played a crucial role in the selectivity towards C_2 olefin [8]. Hence, the production of C_1, C_3, and more complex C_{4+} compounds was hindered.

Both in MTH and ETH reactions, persistent production of ethers, dimethyl, or diethyl, respectively, could be observed either on chromatograms (Figure S4) or mass spectroscopy measurements results (Figure 4c and 4d). The amounts of diethyl ether produced in the ETH reaction were smaller than those of the analogous ether compound in the MTH reaction.

Accordingly, MS results, presented in Figures 4c and 4e, illustrate the MTH process running over the SSZ-13 catalyst. As evidenced by the GC measurement results, MS also showed that catalyst activity decreased. It was reflected in the signal of m/z = 31, belonging to methanol substrate, rising, which was observed after ca. 30 minutes of the reaction, with accompanying decline of signals m/z = 18 related with water; m/z = 27 and 29 assigned to C_2 and C_3 olefinic and paraffinic species; m/z = 56 stemming from butenes as well as m/z = 70 signal, related to C_5 olefinic species. The signal identifying dimethyl ether, i.e., m/z = 45, fluctuated throughout the reaction. The signal peaked after ca. 7 minutes of the reaction, and its fall stopped around the 30-minute mark. This effect was accompanied by the intense rise of the m/z = 27, 41, and 56, representing C_2, C_3, and C_4 olefins, respectively, which meant a reaction acceleration in the presence of dimethyl ether. In the second half of the process, the m/z = 45 signal again rose as consumption of the DME for olefins production slowed down. During the last 30 minutes of the process, another decline was observed, indicating the participation of DME in coke species production.

Results obtained for ETH reaction are depicted in Figures 4d and 4f. Thus, signals of the highest intensity, i.e. m/z = 18 and 27-29, stemming from water and C_2-C_3 olefins/paraffins, respectively, were stable throughout the reaction time. Also, in the second half of the process, signals of m/z = 59 and 74 became visible, together with the increase in the intensity of m/z = 31 and 45. This group of signals corresponded to diethyl ether. Its growth coincided with conversion decline, indicating its participation in the transformations leading to coke species.

Fragmentation ion masses observed during mass spectrometry measurements and their assignments to particular compounds are gathered in Table S1 (Supplementary Material).

3.3. MCR-ALS analysis of FT-IR and UV-Vis spectroscopic data results

MCR-ALS analysis of obtained spectroscopic data provided additional insight into the reaction path and brought a piece of great complementary information, allowing for unraveling transformations during both processes.

Analysis of the IR spectra for methanol transformation allowed for distinguishing five spectral components (Figure 5a), clearly differing in their time evolution. The most important spectral feature of component A, which defined the chemical character of the reaction's first products, was the presence of bands in the 1525-1425 cm^{-1} range, suggesting the formation of unsaturated compounds with C=C bonds, both in isolated, as well as conjugated form (C=C-C=C; C=C=C), i.e. olefins. The appearance of ethylene and propylene was manifested by the 1445 cm^{-1} band of their gas phase (Figure 5a). Signals corresponding to $-CH_3$ group oscillations displayed a complex nature, which was suggested by the

presence of the band stemming from CH_3-O moieties (1418 cm^{-1}), i.e. dimethyl ether. GC measurements confirmed its formation throughout the reaction's whole duration, where small amounts of this compound could be detected at any point of the process. A possible share of dimethyl ether in the IR spectra's C, D, and E components also cannot be excluded. Additional analysis of component A concentration profile (Figure 5b) suggested that olefin production was initiated right at the moment of alcohol contact with the catalyst's surface, reached a maximum after 5 minutes of the process, and then started to decrease successively. The path of component C concentration profile implied its formation at the expense of olefins represented by component B. Spectral characterization of component C indicated that at this stage of the reaction, products became less abundant in olefins (decrease of 1525-1425 cm^{-1} bands), as those transformed into cyclic olefins and/or aromatic species, both types of compounds being highly alkylated with unsaturated substituents (coexistence of 1680-1625 cm^{-1} and 1525-1425 cm^{-1} bands). Right at the beginning of the reaction, described by the component A profile, a sharp, high-intensity band at 1507 cm^{-1} could be observed, which was ascribed to cyclopentenyl cations [10]. The attribution of the 1507 cm^{-1} band was complicated due to the high share of the gas-phase water and ethylene in the spectrum. Nevertheless, the 1507 cm^{-1} band became increasingly visible in the next components, D and E, pointing to the growing share of cyclopentenyl cations in the MTH process. Reaching the maximum concentration of component C, i.e., the formation of a hydrocarbon pool, was connected with the evolution of both components D and E. The development of component E preceded evolution of component D, which suggested transformation of certain number of methylated cyclopentenyl cations into methyl-substituted benzenium cations (based on UV-vis band identified as hexamethylated benzenium cations), which then were transformed into poliaromatic species, that constituted coke deposit responsible for catalysts deactivation. Indeed, after 30 minutes, changes in catalytic reaction yield could be observed, which was related to a decrease in olefins production in favor of dimethyl ether production, also visible in MS results (Figure 4a and 4c). This observation indicated the deactivation of acidic centers. Spectral features of component D, namely the 1507 and 1418 cm^{-1} bands intensities and their ratio, allow for drawing a conclusion that species described by component D had a share of cyclopentenyl species with definitely shorter alkyl substituents than those observed for component C. A share of polyalkylated naphthalenes (1565 cm^{-1}) was identified in component E. This component became dominant, starting at the 40-minute mark of the process. This coking stage of the reaction (component E) was accompanied by xylenes production, identified by 1515 cm^{-1} (p-xylene) and 1602 cm^{-1} (m-xylene) bands.

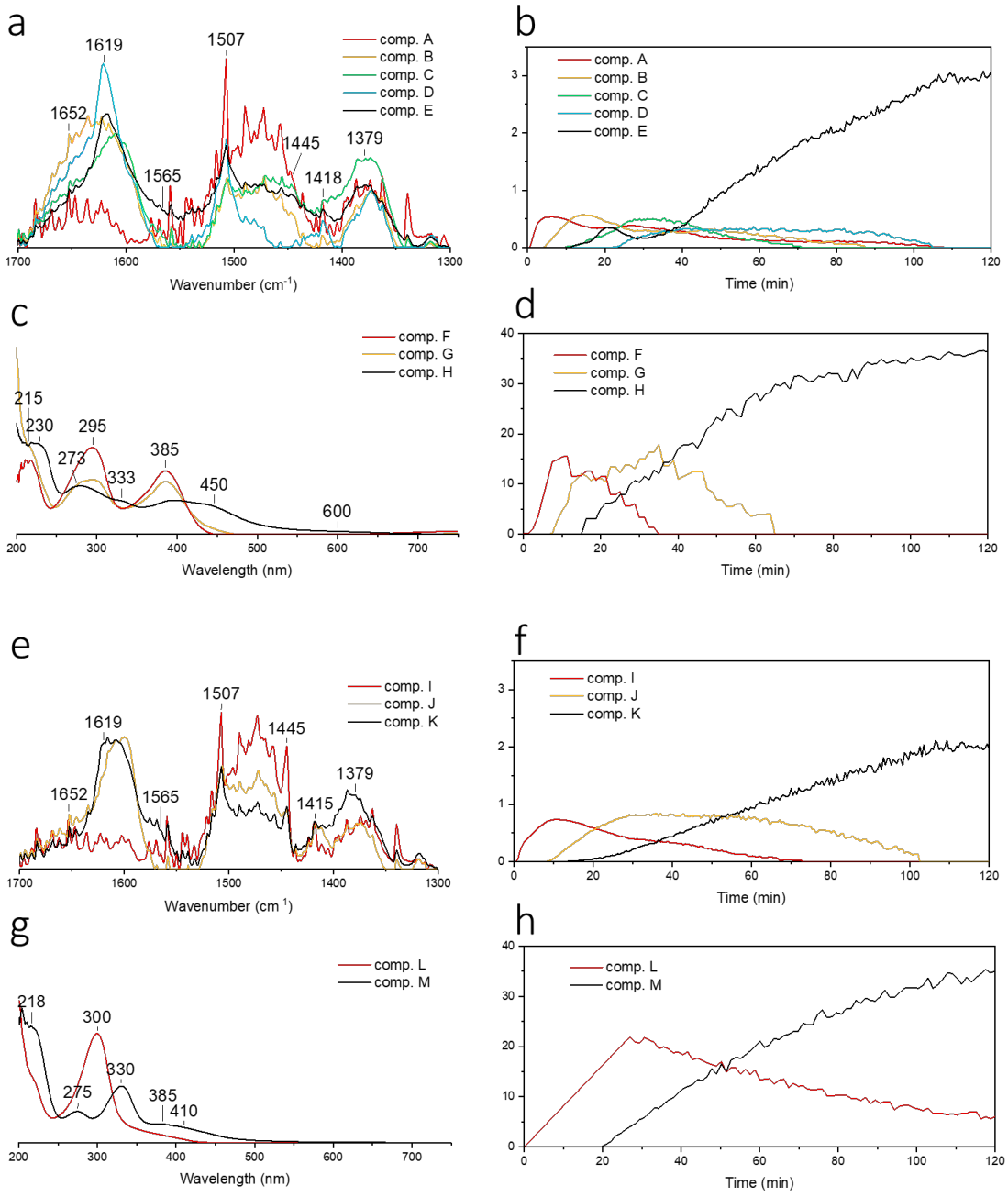

Figure 5 Left column: the MCR-ALS analysis of FT-IR and UV-Vis spectra components recorded during methanol (a, c) and ethanol (e, g) conversion. Right column: corresponding components concentration profiles (b, d, f, and h).

The results described above closely corresponded with the MCR-ALS analysis of UV-Vis spectra (Figure 5c). In component F, related to the first stage of the reaction (Figure 5d), methylated cyclopentenyl cations (10-carbon total) and methylated benzenium cations could be identified, appearing as bands at 295 nm and 385 nm, respectively. The creation of these compounds was correlated with the production of olefins, which is identified by the 215 nm band. In the next stage of the reaction (component G), the production of olefins became elevated, and their diversification was manifested by the appearance of a relevant band in the range of lower wavelengths (<215 nm). Release of high amounts of olefins was correlated with consumption of alkylated cyclopentenyl species (295 nm), while hexamethylated benzenium cations (385 nm) were perturbed to a lower extent. Importantly, in this component, two

types of cyclopentenyl cations were identified, namely the ones with long substituting chains (295 nm), present from the beginning of the reaction, and others with bands occurring at lower wavelengths, disguised under broadened 273 nm band, identifying alkylated cyclopentenyl cations with shorter alkylating chains and/or their lower number. The association of the shift of the alkylated cyclopentenyl cations band with the length of alkylating group chains, as well as their branching, was widely discussed in the literature [10]. This observation pointed out that the release of olefins occurred rather through the conversion of cyclopentenyl and not methylbenzenium species. In the later reaction stage (component H), alkylated cyclopentenyl cations were detected in lower amounts, with shorter alkylating groups (7-carbon total, 273 nm). Polymethylated benzenes were almost completely transformed into highly substituted naphthalenes (450 nm) and trimethylbenzenes (1,2,4- and 1,3,5- TMB, 330 nm). The 230 nm band was related to neutral aromatic species. Also, a decrease in the amount of olefins was observed in the last stage of the reaction (component H).

In the case of ethanol conversion, IR spectra displayed similar bands to those seen in the reaction with methanol, differing mainly with the bands' intensities and their transformation in time. With the aid of MCR-ALS analysis of the IR spectroscopic results, the spectra were divided into three components (Figure 5e). Component I was almost entirely dominated by ethylene (1445 cm^{-1}) and water. Both compounds were identified by sharp bands stemming from their gas phase. Bands corresponding to -CH_3 oscillations were of a complex nature, which again suggested the presence of CH_3-O moieties (1418 cm^{-1}), i.e., diethyl ether, whose presence among reaction products was confirmed throughout its whole duration by GC measurements. Additionally, alkylated cyclopentenyl cations (1507 cm^{-1}) and higher olefins were present in this component. Ethylene, the product of ethanol dehydration, appeared immediately upon the alcohol contact with the catalyst surface, and its production was maintained until the end of the process, as confirmed by the GC and MS measurements during catalytic experiments (Figure 5b and 5d). An analogous situation was observed for the methanol transformation; however, in that case, ethylene and propylene were the products of the C-C coupling reaction. Component I dominated the ETH reaction for 20 minutes, later being substituted by reactants identified in component J (Figure 5f), i.e. alkylated cyclopentenyl cations and benzenium cations. These compounds were produced later in the ETH reaction than observed for MTH conversion. Component J also pointed to producing conjugated olefins (1680-1625 cm^{-1}) in significantly lower amounts than for MTH. Compounds corresponding to component K appeared after 15 minutes of reaction, and their amounts gradually increased for the rest of the process. These were diethyl ether, methyl-substituted naphthalenes, and alkylated aromatics, both latter species considered coke precursors. This effect was accompanied by the slow limiting of olefin production (seen for catalytic results) and the formation of polycyclic aromatic structures, as observed in the GC-MS measurements of extracted coke (Section 3.4).

Similar conclusions could be made based on UV-Vis spectra and their MCR-ALS analysis (Figure 5g). The ethylene (218 nm) production (component L, Figure 5 h) was accompanied by alkylated cyclopentenyl cations (300 nm). The position of the cyclopentenyl cations band at a higher wavelength, observed in component L (300 nm), suggested the presence of fully substituted cyclopentenyl cations (>10-carbon total), e.g. tetramethyl(n-propyl) cyclopentenyl cation, which was detected in the extracted coke analysis (Figure 6). Component M appeared after 20 minutes of the reaction, in a maximum point of component L concentration, indicating consecutive transformation of respective compounds. An intense band below 218 nm pointed to the formation of high amounts of olefins, mainly ethylene, significantly higher than it was in the MTH reaction. This indicated the parallel reaction run, which was ethanol dehydration. The band stemming from highly (m)ethylated benzenium cations (385 nm) was of

low intensity, which suggested low effectivity of the alkylated cyclopentenyl cations expansion process. As a result, limited production of other olefins than ethylene and also polycyclic aromatic species, e.g. naphthalenes (410 nm) as coke precursors, was observed. This was also reflected in less diversified coke components for the ETH reaction than in the MTH case. Similarly, as in the MTH process, substituted cyclopentenyl cations of the lower number of alkylating groups could be distinguished in component M (275 nm) and methyl-substituted benzenium cations (330 nm).

Analysis of the IR and UV-Vis spectra indicated a clearly less complex nature for the ETH reaction than the MTH was seen. This meant lower diversity of the products and, most probably, a more straightforward mechanism of ETH reaction than the MTH one under applied experimental conditions, resulting in given product distributions. While methyl-substituted benzenium cations were present from the first minutes of the MTH reaction, their formation in ETH was strongly hindered. The initiation stage of alkylated cyclopentenyl cations formation was also prolonged for the ETH process. Both effects resulted from competition in acidic sites occupation by alcohol dehydration reaction products and products of alcohol transformations through the hydrocarbon pool mechanism.

The ETH process begins with a C_2 reactant, so interference in creating the first carbon-carbon bond is avoided, which is a subject of debate in the MTH process [8]. A parallel occurrence of the side-chain and paring reaction cycles is highly possible in the MTO reaction [57], while the topology of the catalyst rules the relative extent. Within the MTO process, the paring cycle has little influence on producing light olefins during the MTO reaction over H-SAPO-34 [58]. Our UV-Vis and IR data indicate that the mechanism of the ETH process should not be regarded as precisely identical to that of the MTH process. This supports the results of Chowdhury et al. [59], who reported multiple (m)ethylated aromatics as the active HCP species, forming higher olefins. The limited production of hexaalkylated benzenium ions, which are essential for both side-chain and pairing cycles, adversely impacts the formation of $C_{3=}$. During the ETH process, the hexaalkyl-substituted benzenes were detected in small quantities. This was followed by low selectivity for propylene; however, a significant contribution from the alkylated cyclopentenyl ions was seen. Conversely, in the MTH process, a high share of propylene was followed by a high abundance of hexaalkyl-substituted benzenes and alkylated cyclopentenyl ions. The pairing cycle is hindered after the release of propylene from alkylated cyclopentenyl ions, producing less alkyl-substituted benzenes; hence, the side-chain pathway is significantly impeded for the ETH process.

3.4. Analysis of coke deposit by means of GC-MS measurements of extracted species

Coke analysis was performed by means of GC-MS measurements of extracted carbonaceous deposits from spent catalysts. TG analysis allowed for the quantification of deposited coke after the reactions. Obtained chromatograms with compound assignments are presented in Figure 6 (Method 1 – Table S2).

Results demonstrated that more complex coke species that eluted with higher retention times were formed preferentially during the MTH process over the SSZ-13 catalyst. These included polycyclic alkylated compounds, both aromatic and non-aromatic, with intricate functional groups attached. The ethyl functional group was found only in the ethanol-derived coke, while after methanol conversion, the methyl functional group was preferred, understandably. Interestingly, five-atomic compounds were found in both ETH and MTH coke, slightly differing in the alkylating groups attached. These were 5-(1-methylethylidene)-1,3-cyclopentadiene in ETH-derived coke and 1,2,3,4-tetramethyl-5-methylene-1,3-cyclopentadiene in MTH-derived coke. Also, species as large as anthracene were found. Alkylated azulene and benzocycloheptatriene could be detected for MTH and ETH coke, respectively. Also, adamantane and adamantane derivatives were detected in MTH coke. Standard hydrocarbons, expected in both MTH and ETH reactions, such as benzene, naphthalene, and their alkylated derivatives,

contributed to the most excessive amounts of extracted coke. Tetra- and pentamethylbenzenes are found to be more profound in coke species in ETH. Tetramethylbenzene is a highly undesired side-product rarely detected during the zeolite-catalyzed ETH process [59]. It can be concluded that more coke species, including more bulky compounds, could be detected for the MTH reaction remaining. This stayed in accordance with the observed GC measurements of faster catalyst deactivation during methanol conversion. As the coking phase started earlier than it happened for the ETH reaction, together with smaller C_1 building blocks, more complex structures could be created in spacious chabazite cages. Additionally, confirming the spectroscopic-based observations, five-ring compounds were detected in rather small amounts among coke species. Also, the UV and IR spectra concluded that more benzenium ions were formed in the MTH reaction, which was reflected in coke components.

The three major deactivation pathways in the ETH process are the oligomerization, cyclization, and isomerization of ethyl-substituted benzenes. The poly/fused-aromatic-based species are considered the primary deactivating species. These polyaromatic compounds are the precursors of pyrene, which is well-established as the main coke species in zeolite catalysis [60-62], [48]. In the course of this study, more pyrenes were detected after the MTH reaction (Figure S5; Method 2 – Table S2).

After the 2-hour reaction step, the catalyst surface was purged with inert gas to evaluate the remaining coke. Spectra registered after methanol conversion (Figure S2a) displayed 1569 and 1414 cm^{-1} bands, indicating the expected naphthalenic coke species. This supported observations made based on FT-IR measurements during the reaction.

TG analysis provided information on the amount of coke obtained after both reactions. The calculated coke content was 21% and 17% for methanol and ethanol transformations on the SSZ-13 catalyst. Observations stayed in accordance with GC measurements of desorbed products of reactions, with the highest conversion drop during the MTH process due to extensive coking of the catalyst. The observation of a wide distribution of products of MTH reactions led to a broader distribution of coking species, as observed in GC-MS extracted coke analysis.

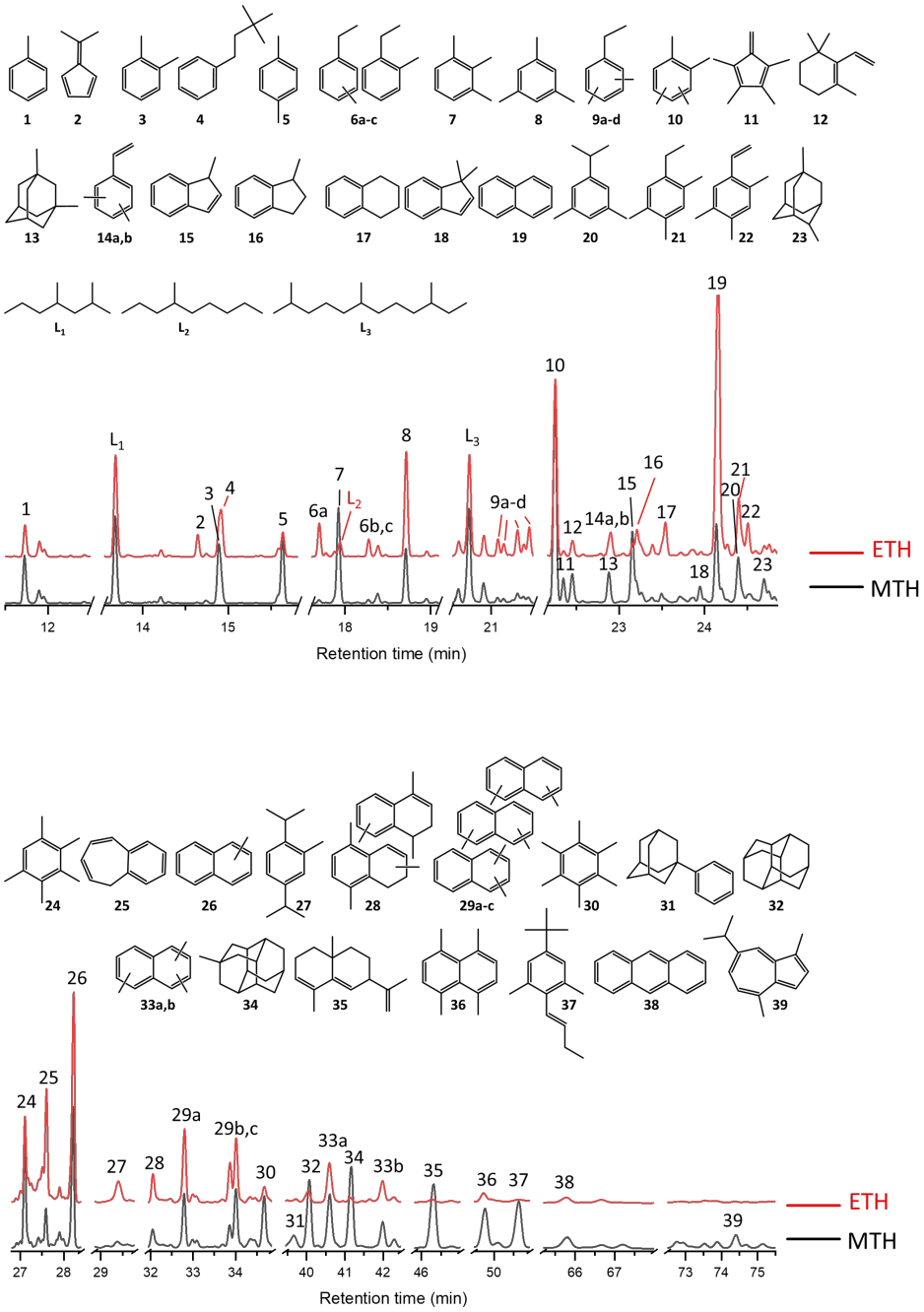

Figure 6 GC-MS analysis of coke species extracted from used catalysts after methanol and ethanol conversion.

4. Conclusions

The operando methodology utilized for examining MTH and ETH processes inside the same zeolite structure as the catalyst facilitated a more comprehensive understanding of reaction pathways by finding intermediate species and ultimately suggesting potential routes for both alcohol conversions. In the MTH process, two intermediate species, alkylated cyclopentenyl, and highly alkylated benzenium ions, were identified as more effective in activating the HCP mechanism, yielding a broader product distribution. The MTH process also exhibited more advanced coking, resulting in accelerated degradation of the SSZ-13 catalyst.

In contrast to the MTH reaction, the ETH method is characterized by exceptionally high selectivity for ethylene. A reduced quantity of coke precursors was generated, and the catalyst exhibited a markedly slower deactivation rate. Infrared spectroscopy demonstrated that methylated benzenium cation must be regarded as the intermediate species influencing HCP cycles, although this was not as evident from UV-Vis analysis. The principal mechanism of ethanol conversion is the dehydration pathway, although HCP exerts a minor influence.

Acknowledgment

This research was funded by the National Science Centre, Poland (Grant No. 2021/41/B/ST4/00048). MCR-ALS analysis results were funded by the National Science Centre, Poland (Grant No. 2023/49/B/ST4/02340). The research was partially carried out using research infrastructure purchased with the funds of the European Union in the framework of the Smart Growth Operational Programme, Measure 4.2; Grant No. POIR.04.02.00-00-D001/20-00, "ATOMIN 2.0 – ATOMic scale science for the INnovative economy".

CRediT authorship contribution statement

A.W.: Writing – original draft, Investigation, Validation, Data curation. K.A.T.: Conceptualisation, Methodology, Writing – review & editing, Validation, Investigation, Data curation, Project administration, Funding acquisition. A.K.: Writing – original draft, Investigation, Data curation, A.O.: Investigation, Data curation; O.R.: Investigation, Data curation; K.G.M.: Writing – review & editing, Project administration, Methodology, Investigation, Funding acquisition, Data curation, Conceptualization.

Data Availability

The link to shared data was added at the Attach Filestep.

"UV-Vis and FT-IR operando studies of methanol and ethanol transformation on zeolite HSZZ-13 - replication data" (https://doi.org/10.57903/UJ/K97TB5).

References

[1] S.A. Chernyak, M. Corda, J.-P. Dath, V.V. Ordomsky, A.Y. Khodakov, Light olefin synthesis from a diversity of renewable and fossil feedstocks: state-of the-art and outlook, Chemical Society Reviews, 51 (2022) 7994-8044.

[2] I. Yarulina, A.D. Chowdhury, F. Meirer, B.M. Weckhuysen, J. Gascon, Recent trends and fundamental insights in the methanol-to-hydrocarbons process, Nature Catalysis, 1 (2018) 398-411.

[3] F. Dalena, A. Senatore, A. Marino, A. Gordano, M. Basile, A. Basile, Chapter 1 - Methanol Production and Applications: An Overview, in: A. Basile, F. Dalena (Eds.) Methanol, Elsevier2018, pp. 3-28.

[4] L. Bhatia, S. Johri, R. Ahmad, An economic and ecological perspective of ethanol production from renewable agro waste: a review, AMB Express, 2 (2012) 65.

[5] A.D. Chowdhury, A.L. Paioni, K. Houben, G.T. Whiting, M. Baldus, B.M. Weckhuysen, Bridging the Gap between the Direct and Hydrocarbon Pool Mechanisms of the Methanol-to-Hydrocarbons Process, Angewandte Chemie International Edition, 57 (2018) 8095-8099.

[6] R. Johansson, S.L. Hruby, J. Rass-Hansen, C.H. Christensen, The Hydrocarbon Pool in Ethanol-to-Gasoline over HZSM-5 Catalysts, Catalysis Letters, 127 (2009) 1-6.

[7] S. Ilias, A. Bhan, Mechanism of the Catalytic Conversion of Methanol to Hydrocarbons, ACS Catalysis, 3 (2013) 18-31.

[8] S. Zeng, W. Zhang, J. Li, S. Lin, S. Xu, Y. Wei, Z. Liu, Revealing the roles of hydrocarbon pool mechanism in ethanol-to-hydrocarbons reaction, Journal of Catalysis, 413 (2022) 517-526.

[9] I.M. Dahl, S. Kolboe, On the reaction mechanism for propene formation in the MTO reaction over SAPO-34, Catalysis Letters, 20 (1993) 329-336.

[10] E.D. Hernandez, F.C. Jentoft, Spectroscopic Signatures Reveal Cyclopentenyl Cation Contributions in Methanol-to-Olefins Catalysis, ACS Catalysis, 10 (2020) 5764-5782.

[11] M.J. Wulfers, F.C. Jentoft, The Role of Cyclopentadienium Ions in Methanol-to-Hydrocarbons Chemistry, ACS Catalysis, 4 (2014) 3521-3532.

[12] C. Wang, J. Xu, G. Qi, Y. Gong, W. Wang, P. Gao, Q. Wang, N. Feng, X. Liu, F. Deng, Methylbenzene hydrocarbon pool in methanol-to-olefins conversion over zeolite H-ZSM-5, Journal of Catalysis, 332 (2015) 127-137.

[13] S. Svelle, M. Bjørgen, S. Kolboe, D. Kuck, M. Letzel, U. Olsbye, O. Sekiguchi, E. Uggerud, Intermediates in the Methanol-to-hydrocarbons (MTH) Reaction: A Gas Phase Study of the Unimolecular Reactivity of Multiply Methylated Benzenium Cations, Catalysis Letters, 109 (2006) 25-35.

[14] M.R. Gogate, Methanol-to-olefins process technology: current status and future prospects, Petroleum Science and Technology, 37 (2019) 559-565.

[15] J. Sun, Y. Wang, Recent Advances in Catalytic Conversion of Ethanol to Chemicals, ACS Catalysis, 4 (2014) 1078-1090.

[16] M. Yang, D. Fan, Y. Wei, P. Tian, Z. Liu, Recent Progress in Methanol-to-Olefins (MTO) Catalysts, Advanced Materials, 31 (2019) 1902181.

[17] M. Zhang, Y. Yu, Dehydration of Ethanol to Ethylene, Industrial & Engineering Chemistry Research, 52 (2013) 9505-9514.

[18] W. Xia, C. Ma, Y. Huang, S. Li, X. Wang, K. Chen, D. Liu, Bioethanol Conversion into Propylene over Various Zeolite Catalysts: Reaction Optimization and Catalyst Deactivation, Nanomaterials, 2022.

[19] L. Wu, T. Zhou, Q. Cui, H. Wang, Y. Hu, H. Huang, The Catalytic Dehydration of Bio-ethanol to Ethylene on SAPO-34 Catalysts, Petroleum Science and Technology, 31 (2013) 2414-2421.

[20] T.K. Phung, L. Proietti Hernández, A. Lagazzo, G. Busca, Dehydration of ethanol over zeolites, silica alumina and alumina: Lewis acidity, Brønsted acidity and confinement effects, Applied Catalysis A: General, 493 (2015) 77-89.

[21] Z.S.B. Sousa, C.O. Veloso, C.A. Henriques, V. Teixeira da Silva, Ethanol conversion into olefins and aromatics over HZSM-5 zeolite: Influence of reaction conditions and surface reaction studies, Journal of Molecular Catalysis A: Chemical, 422 (2016) 266-274.

[22] C.-Y. Wu, H.-S. Wu, Ethylene Formation from Ethanol Dehydration Using ZSM-5 Catalyst, ACS Omega, 2 (2017) 4287-4296.

[23] K. Hemelsoet, A. Ghysels, D. Mores, K. De Wispelaere, V. Van Speybroeck, B.M. Weckhuysen, M. Waroquier, Experimental and theoretical IR study of methanol and ethanol conversion over H-SAPO-34, Catalysis Today, 177 (2011) 12-24.

[24] Q. Qian, J. Ruiz-Martínez, M. Mokhtar, A.M. Asiri, S.A. Al-Thabaiti, S.N. Basahel, H.E. van der Bij, J. Kornatowski, B.M. Weckhuysen, Single-Particle Spectroscopy on Large SAPO-34 Crystals at Work: Methanol-to-Olefin versus Ethanol-to-Olefin Processes, Chemistry – A European Journal, 19 (2013) 11204-11215.

[25] E.T.C. Vogt, D. Fu, B.M. Weckhuysen, Carbon Deposit Analysis in Catalyst Deactivation, Regeneration, and Rejuvenation, Angewandte Chemie International Edition, 62 (2023) e202300319.

[26] E.C. Nordvang, E. Borodina, J. Ruiz-Martínez, R. Fehrmann, B.M. Weckhuysen, Effects of Coke Deposits on the Catalytic Performance of Large Zeolite H-ZSM-5 Crystals during Alcohol-to-Hydrocarbon Reactions as Investigated by a Combination of Optical Spectroscopy and Microscopy, Chemistry – A European Journal, 21 (2015) 17324-17335.

[27] M. Luo, H. Zang, B. Hu, B. Wang, G. Mao, Evolution of confined species and their effects on catalyst deactivation and olefin selectivity in SAPO-34 catalyzed MTO process, RSC Advances, 6 (2016) 17651-17658.

[28] S. Gao, S. Xu, Y. Wei, Q. Qiao, Z. Xu, X. Wu, M. Zhang, Y. He, S. Xu, Z. Liu, Insight into the deactivation mode of methanol-to-olefins conversion over SAPO-34: Coke, diffusion, and acidic site accessibility, Journal of Catalysis, 367 (2018) 306-314.

[29] L. Pinard, K.B. Tayeb, S. Hamieh, H. Vezin, C. Canaff, S. Maury, O. Delpoux, Y. Pouilloux, On the involvement of radical “coke” in ethanol conversion to hydrocarbons over HZSM-5 zeolite, Catalysis Today, 218-219 (2013) 57-64.

[30] Q. Qian, C. Vogt, M. Mokhtar, A.M. Asiri, S.A. Al-Thabaiti, S.N. Basahel, J. Ruiz-Martínez, B.M. Weckhuysen, Combined Operando UV/Vis/IR Spectroscopy Reveals the Role of Methoxy and Aromatic Species during the Methanol-to-Olefins Reaction over H-SAPO-34, ChemCatChem, 6 (2014) 3396-3408.

[31] E. Borodina, H. Sharbini Harun Kamaluddin, F. Meirer, M. Mokhtar, A.M. Asiri, S.A. Al-Thabaiti, S.N. Basahel, J. Ruiz-Martinez, B.M. Weckhuysen, Influence of the Reaction Temperature on the Nature of the Active and Deactivating Species During Methanol-to-Olefins Conversion over H-SAPO-34, ACS Catalysis, 7 (2017) 5268-5281.

[32] J. Goetze, F. Meirer, I. Yarulina, J. Gascon, F. Kapteijn, J. Ruiz-Martínez, B.M. Weckhuysen, Insights into the Activity and Deactivation of the Methanol-to-Olefins Process over Different Small-Pore Zeolites As Studied with Operando UV–vis Spectroscopy, ACS Catalysis, 7 (2017) 4033-4046.

[33] S.A. Kadam, M.V. Shamzhy, IR Operando Study of Ethanol Dehydration over MFI Zeolites: Structure–Activity Relationships, The Journal of Physical Chemistry C, 122 (2018) 24055-24067.

[34] S.H. van Vreeswijk, M. Monai, R. Oord, J.E. Schmidt, E.T.C. Vogt, J.D. Poplawsky, B.M. Weckhuysen, Nano-scale insights regarding coke formation in zeolite SSZ-13 subject to the methanol-to-hydrocarbons reaction, Catalysis Science & Technology, 12 (2022) 1220-1228.

[35] Q. Qian, J. Ruiz-Martínez, M. Mokhtar, A.M. Asiri, S.A. Al-Thabaiti, S.N. Basahel, B.M. Weckhuysen, Single-Particle Spectroscopy of Alcohol-to-Olefins over SAPO-34 at Different Reaction Stages: Crystal Accessibility and Hydrocarbons Reactivity, ChemCatChem, 6 (2014) 772-783.

[36] C.J. Van Oers, K. Gora-Marek, B. Prelot, J. Datka, V. Meynen, P. Cool, Demonstrating the Benefits and Pitfalls of Various Acidity Characterization Techniques by a Case Study on Bimodal Aluminosilicates, Langmuir, 30 (2014) 1880-1887.

[37] J. Jaumot, R. Gargallo, A. de Juan, R. Tauler, A graphical user-friendly interface for MCR-ALS: a new tool for multivariate curve resolution in MATLAB, Chemometrics and Intelligent Laboratory Systems, 76 (2005) 101-110.

[38] J. Jaumot, A. de Juan, R. Tauler, MCR-ALS GUI 2.0: New features and applications, Chemometrics and Intelligent Laboratory Systems, 140 (2015) 1-12.

[39] A. de Juan, J. Jaumot, R. Tauler, Multivariate Curve Resolution (MCR). Solving the mixture analysis problem, Analytical Methods, 6 (2014) 4964-4976.

[40] K. De Wispelaere, C.S. Wondergem, B. Ensing, K. Hemelsoet, E.J. Meijer, B.M. Weckhuysen, V. Van Speybroeck, J. Ruiz-Martínez, Insight into the Effect of Water on the Methanol-to-Olefins Conversion in H-SAPO-34 from Molecular Simulations and in Situ Microspectroscopy, ACS Catalysis, 6 (2016) 1991-2002.

[41] S. Bailleul, I. Yarulina, A.E.J. Hoffman, A. Dokania, E. Abou-Hamad, A.D. Chowdhury, G. Pieters, J. Hajek, K. De Wispelaere, M. Waroquier, J. Gascon, V. Van Speybroeck, A Supramolecular View on the Cooperative Role of Brønsted and Lewis Acid Sites in Zeolites for Methanol Conversion, Journal of the American Chemical Society, 141 (2019) 14823-14842.

[42] T. Omojola, A.J. Logsdail, A.C. van Veen, S.A.F. Nastase, A quantitative multiscale perspective on primary olefin formation from methanol, Physical Chemistry Chemical Physics, 23 (2021) 21437-21469.

[43] K.A. Tarach, A.K. Walczyk, A. Kordek, O. Rogala, K. Góra-Marek, Silver-Loaded Chabazite in Ethanol-to-Hydrocarbon Process—Operando FT-IR and UV-Vis Spectroscopic Studies, Molecules, 2024.

[44] W. Zhang, Y. Zhi, J. Huang, X. Wu, S. Zeng, S. Xu, A. Zheng, Y. Wei, Z. Liu, Methanol to Olefins Reaction Route Based on Methylcyclopentadienes as Critical Intermediates, ACS Catalysis, 9 (2019) 7373-7379.

[45] W. Zhang, M. Zhang, S. Xu, S. Gao, Y. Wei, Z. Liu, Methylcyclopentenyl Cations Linking Initial Stage and Highly Efficient Stage in Methanol-to-Hydrocarbon Process, ACS Catalysis, 10 (2020) 4510-4516.

[46] K. Van der Borght, R. Batchu, V.V. Galvita, K. Alexopoulos, M.-F. Reyniers, J.W. Thybaut, G.B. Marin, Insights into the Reaction Mechanism of Ethanol Conversion into Hydrocarbons on H-ZSM-5, Angewandte Chemie International Edition, 55 (2016) 12817-12821.

[47] M. Bjørgen, F. Bonino, S. Kolboe, K.-P. Lillerud, A. Zecchina, S. Bordiga, Spectroscopic Evidence for a Persistent Benzenium Cation in Zeolite H-Beta, Journal of the American Chemical Society, 125 (2003) 15863-15868.

[48] L. Pinard, S. Hamieh, C. Canaff, F. Ferreira Madeira, I. Batonneau-Gener, S. Maury, O. Delpoux, K. Ben Tayeb, Y. Pouilloux, H. Vezin, Growth mechanism of coke on HBEA zeolite during ethanol transformation, Journal of Catalysis, 299 (2013) 284-297.

[49] M. Bjørgen, F. Bonino, B. Arstad, S. Kolboe, K.-P. Lillerud, A. Zecchina, S. Bordiga, Persistent Methylbenzenium Ions in Protonated Zeolites: The Required Proton Affinity of the Guest Hydrocarbon, ChemPhysChem, 6 (2005) 232-235.

[50] X.-Z. Jiang, In situ FTIR studies of extraframework aluminum bound methoxy species in H-ZSM-5 zeolites, Journal of Molecular Catalysis A: Chemical, 121 (1997) 63-68.

[51] M. Arivazhagan, V.P. Subhasini, R. Kavitha, R. Senthilkumar, The spectroscopic (FT-IR, FT-Raman), MESP, first order hyperpolarizability, NBO analysis, HOMO and LUMO analysis of 1,5-dimethyl napthalene by density functional method, Spectrochimica Acta Part A: Molecular and Biomolecular Spectroscopy, 131 (2014) 636-646.

[52] S.R. Langhoff, Theoretical Infrared Spectra for Polycyclic Aromatic Hydrocarbon Neutrals, Cations, and Anions, The Journal of Physical Chemistry, 100 (1996) 2819-2841.

[53] L. Maggiulli, V.L. Sushkevich, O. Kröcher, J.A. van Bokhoven, D. Ferri, Correlating the Nature of Carbenium Ions in Zeolites to the Product Distribution in the Methanol-to-Olefins Process, ACS Catalysis, 14 (2024) 11477-11489.

[54] G.B. Lebron, T.L. Tan, Integrated Band Intensities of Ethylene () by Fourier Transform Infrared Spectroscopy, International Journal of Spectroscopy, 2012 (2012) 474639.

[55] J.W. Park, G. Seo, IR study on methanol-to-olefin reaction over zeolites with different pore structures and acidities, Applied Catalysis A: General, 356 (2009) 180-188.

[56] L. Qi, J. Li, Y. Wei, L. Xu, Z. Liu, Role of naphthalene during the induction period of methanol conversion on HZSM-5 zeolite, Catalysis Science & Technology, 6 (2016) 3737-3744.

[57] S. Xu, A. Zheng, Y. Wei, J. Chen, J. Li, Y. Chu, M. Zhang, Q. Wang, Y. Zhou, J. Wang, F. Deng, Z. Liu, Direct Observation of Cyclic Carbenium Ions and Their Role in the Catalytic Cycle of the Methanol-to-Olefin Reaction over Chabazite Zeolites, Angewandte Chemie International Edition, 52 (2013) 11564-11568.

[58] C.-M. Wang, Y.-D. Wang, H.-X. Liu, Z.-K. Xie, Z.-P. Liu, Theoretical insight into the minor role of paring mechanism in the methanol-to-olefins conversion within HSAPO-34 catalyst, Microporous and Mesoporous Materials, 158 (2012) 264-271.

[59] A.D. Chowdhury, A. Lucini Paioni, G.T. Whiting, D. Fu, M. Baldus, B.M. Weckhuysen, Unraveling the Homologation Reaction Sequence of the Zeolite-Catalyzed Ethanol-to-Hydrocarbons Process, Angewandte Chemie International Edition, 58 (2019) 3908-3912.

[60] K. Moljord, P. Magnoux, M. Guisnet, Pyrene oxidation as a model reaction for characterizing the mechanism of coke oxidation on Y zeolites, Catalysis Letters, 28 (1994) 53-59.

[61] S.M. Holmes, A. Garforth, J. Dwyer, Pyrolysis GC-MS study of external coke composition on H-ZSM-5 zeolite catalysts, Thermochimica Acta, 294 (1997) 57-64.

[62] E. Borodina, F. Meirer, I. Lezcano-González, M. Mokhtar, A.M. Asiri, S.A. Al-Thabaiti, S.N. Basahel, J. Ruiz-Martinez, B.M. Weckhuysen, Influence of the Reaction Temperature on the Nature of the

1 Active and Deactivating Species during Methanol to Olefins Conversion over H-SSZ-13, ACS Catalysis, 5
2 (2015) 992-1003.

3